Prepared for submission to JCAP

UHECR mass composition at highest energies from anisotropy of their arrival directions

M.Yu. Kuznetsov,[a,b] **P.G. Tinyakov**[a,b]

[a]Universite Libre de Bruxelles, Brussels, 1000, Belgium
[b]Institute for Nuclear Research of the Russian Academy of Sciences, Moscow, 117312, Russia

E-mail: mkuzn@inr.ac.ru

Abstract. We propose a new method for the estimation of ultra-high energy cosmic ray (UHECR) mass composition from a distribution of their arrival directions. The method employs a test statistic (TS) based on a characteristic deflection of UHECR events with respect to the distribution of luminous matter in the local Universe. Making realistic simulations of the mock UHECR sets, we show that this TS is robust to the presence of regular Galactic magnetic field and sensitive to the mass composition of events in a set. This allows one to constrain the UHECR mass composition by comparing the TS distribution of a composition model in question with the data TS, and to discriminate between different composition models. While the statistical power of the method depends somewhat on the GMF parameters, this dependence decreases with the growth of statistics. The method shows good performance even at GZK energies where the estimation of UHCER mass composition with traditional methods is complicated by a low statistics.

Keywords: ultra-high energy cosmic rays, large scale structure, anisotropy, mass composition

Contents

1 Introduction

Despite the experimental progress in detection of ultra-high energy cosmic rays (UHECR) and growing quality and quantity of data, our understanding of this phenomenon is hampered by three coupled unsolved problems: UHECR sources, nature of UHECR particles and cosmic magnetic fields.

Identification of sources of UHECR from their sky distribution is not straightforward. While the arrival directions of incident particles are reconstructed quite accurately — with the precision of $1 - 1.5^\circ$ and no systematic errors, the directions to the UHECR sources cannot be determined with any precision because UHECR are likely to be charged particles and are thus deflected in cosmic magnetic fields by potentially much larger angles. These deflections are uncertain because of both the unknown particle charge and uncertainties in the magnetic fields.

For their tiny flux, UHECR are only observed indirectly through extensive air showers they produce in the atmosphere. This makes determining the nature (and therefore the charge) of their primary particles prone to uncertainties of hadronic interaction models. The existing measurements [1–4] have large errors and may contain unknown systematic effects.

Cosmic magnetic fields are also not known sufficiently well. Experimentally, only loose bounds exist on the extragalactic fields: it is constrained by 10^{-15} G from below [5, 6] and by 10^{-9} G from above [7]. However, the arguments based on structure formation and measured fields in galaxy clusters indicate that the field in the voids should not be much larger than $\sim 10^{-12}$ G, in which case the deflections of cosmic rays

in voids are negligible [8], and sizable extragalactic deflections may only arise either close to the source or close to our galaxy if it is itself a part of a filament [9] with sizeable magnetic fields.

A rough magnitude of the coherent Galactic magnetic field (GMF) is known to be several μG from Faraday rotation measures of extragalactic sources and from other observations [10]. However, its general structure is unknown because reconstruction of a 3d field from a 2d projection is ambiguous. Several proposed phenomenological models [11–14] should be considered as examples of what the field might be, at best. This makes it impossible to reconstruct the directions to the UHECR sources with any certainty and trace where particular UHECRs have come from.

The arrival directions of observed UHECR events do not give any obvious indication of the nature of sources. The existing data appear quite isotropic, with no significant small scale clustering found so far, and little large scale structure: there has been a dipole of 6% detected at intermediate energies of 8 EeV [15], and a concentrations of events — the "hot spots" of the radius of $\sim 25^\circ$ — at high energies above 57 EeV [16], with the significance requiring further confirmation. Such remarkable isotropy, together with a short propagation distance of all known charged particles at highest energies, suggests deflections of at least a few tens of degrees for the bulk of UHECR even at highest energies.

In the absence of a clear hypothesis of what UHECR are and where they come from, one may opt for narrowing the search by excluding models. For this approach to be useful three uncertainties — sources, composition and magnetic fields — have to be somehow reduced to a manageable set by additional assumptions. A most robust assumption can be made about the source distribution in space: in all existing models they follow the matter distribution. If one assumes in addition that the sources are sufficiently numerous to be treated on statistical basis, the uncertainty related to sources is essentially eliminated. We will refer to this source distribution as Large-scale Structure (LSS) source model. This approach has already been used in previous studies. For example, the lack of anisotropy in the data together with the rough magnitude of GMF appears to be in tension with pure proton models [17].

The unknown composition affects the distribution of arrival directions in two ways: through the attenuation of UHECR, and through deflections in magnetic fields. The situation here is under better control since for any type of nuclei the attenuation can be calculated using available propagation codes [18–20], so for any assumed spectrum and composition at the source the spectrum and composition at the detector can be calculated. If not for the uncertainty in magnetic fields, the sky distribution of the events would have been calculable as well. Comparing observed and predicted sky distributions would then allow one to constrain possible UHECR compositions or even, if no good fit is found, to rule out the LSS source model.

In this paper we show that this logic largely survives the uncertainties of the magnetic fields, and propose a method that allows one to constrain the charge composition of UHECR from a distribution of their arrival directions. To understand the idea imagine for the moment that UHECR deflections were purely random. In this case they would be characterized by a single parameter, the width of the Gaussian spread of a

point source. To obtain the prediction of a given model one could then calculate the distribution of arrival directions at zero magnetic field and smear it with the Gaussian function of a given width. Comparing the result to observations one would determine/constrain the likely values of the smearing angle and, given the rough magnitude of magnetic fields, the composition models.

The real magnetic field is not random as there is a coherent field in the Galaxy whose contribution to deflections is likely large, and which is characterized my much more than one parameter even in simplest models. However, one can still define a single observable which has a meaning of a typical deflection angle and which is robust to the presence of a regular Galactic field in the sense of being insensitive to its details, but still sensitive to the overall magnitude of deflections. We propose such an observable below and investigate its discriminative power with respect to different compositions of UHECR.

The rest of this paper is organized as follows: in Section 2 we introduce the likelihood function and the test statistic (TS) that are the main analysis tools of this study. In Section 3 we describe the details of simulations of mock UHECR event sets, including assumptions made about source distribution, UHECR composition, propagation and deflections in magnetic fields. In Section 4 we check the accuracy and robustness of reconstruction of UHECR flux parameters with this TS. Making use of the simulated TS distributions, in Section 5 we formulate and test the method to constrain the UHECR mass composition and to compare different composition models. We also discuss the impact of magnetic field uncertainties and energy threshold variation on the results. We present our conclusions in Section 6.

2 The choice of test statistics and observable

The key ingredient of our proposal is the choice of the test statistics and the corresponding observable. To distinguish between different compositions, we want it to depend on the overall magnitude of deflections but be insensitive to their particular directions. One may expect that such observable will not depend strongly on the details of the coherent magnetic field, but mainly on its overall magnitude — the latter is the parameter best known from observations. Note that the existing GMF models agree on the overall magnitude of the Galactic field within $\sim 50\%$, which has smaller effect on deflections than the uncertainty in the particle charge which ranges from 1 for protons to 26 for iron. One may thus expect to constrain the composition despite the relatively poor knowledge of the magnetic field.

Our choice of observable is inspired by the case of purely random deflections which are characterized by a single parameter, the width of the Gaussian spread of a point source. By analogy, we choose to characterise the given set of arrival deflections by its typical deflection angle with respect to the LSS source model. Given the set of events, this quantity is calculated as follows.

For a given smearing parameter θ we construct the sky map of the expected flux making use of the source distribution in space and the exposure of the experiment (the procedure is described in detail in Sec. 3). We characterize this flux by a flux

map $\Phi(\theta, \mathbf{n})$ — a continuous function of the direction, which is normalized to a unit integral over the sphere so that it can be interpreted as a probability density to observe an event from the direction $\mathbf{n}$.

Given the flux map $\Phi(\theta, \mathbf{n})$ it is straightforward to generate the set of events that follow the corresponding distribution by throwing random events and accepting them with the probability $\Phi(\theta, \mathbf{n})$ according to their direction $\mathbf{n}$. Inversely, given the set of events with directions $\mathbf{n}_i$ generated with some value of θ, one can determine the value of θ by computing the θ-dependent likelihood function

$$\mathcal{L}(\theta) = \sum_i \ln \frac{\Phi(\theta, \mathbf{n}_i)}{\Phi_{\rm iso}(\mathbf{n}_i)} \tag{2.1}$$

and finding its maximum with respect to θ. Here for convenience we have chosen the normalization factor $\Phi_{\rm iso}(\mathbf{n}_i) = \Phi(\infty, \mathbf{n}_i)$ that corresponds to the isotropic distribution of sources — a uniform flux modulated by the exposure function.

So far we have assumed that all CR events are deflected in the same way, while in a realistic situation the events have different energies. Accounting for the energy dependence does not introduce additional parameters as the deflection angles are inversely proportional to event energies and can be expressed in terms of a single parameter, e.g. the deflection at a reference energy $E_0 = 100$ EeV. We bin the energies in log-uniform intervals with lower boundaries E_k (ten bins per energy decade with the highest bin an open interval $E > 180$ EeV) and neglect the energy dependence within each bin. We then define a flux map $\Phi_k(\theta, \mathbf{n})$ in each energy bin. Note that the attenuation of cosmic rays is energy-dependent, so the flux maps $\Phi_k(\theta, \mathbf{n})$ at different k differ not only by the deflection angle, and in general $\Phi_k(\theta, \mathbf{n}) \neq \Phi_i(\theta E_i/E_k, \mathbf{n})$.

Generalizing Eq. (2.1) to the case of several energy bins, we finally define our test statistics $TS(\theta)$ as follows:

$$TS(\theta) = -2 \sum_k \left(\sum_i \ln \frac{\Phi_k(\theta, \mathbf{n}_i)}{\Phi_{\rm iso}(\mathbf{n}_i)} \right), \tag{2.2}$$

where the internal sum runs over the events in the energy bin k and we have included a standard normalization factor -2. In the limit of a large number of events, this test statistics is distributed around its minimum according to χ^2-distribution with one degree of freedom.

By definition, the test statistics $TS(\theta)$ is calculated using the LSS source model. As already mentioned, it also implicitly depends on the attenuation of cosmic rays. We adopt the proton attenuation function when calculating the flux maps $\Phi_k(\theta, \mathbf{n})$. In principle this choice is arbitrary. Note, however, that protons attenuate less than other particles, so the maps $\Phi_k(\theta, \mathbf{n})$ calculated with proton attenuation are closer to being isotropic and thus this choice is conservative.

On the contrary, Eq. (2.2) makes no reference to any magnetic field model. Moreover, its sensitivity to the coherence of the field is reduced: for instance, for a single point source the value of $TS(\theta)$ is the same for events spread on the circle around the

source as would be the case for random deflections, or events concentrated in one point on the circle as in the case of a coherent field.

The observable we propose to characterize a given set of events is the value of θ for which the $TS(\theta)$ is minimum. In what follows we call this value $\theta_{\rm rec}$ for "reconstructed". It has the interpretation of the typical deflection angle with respect to the LSS source model at the reference energy $E_0 = 100$ EeV. Its uncertainty is determined by the width of the minimum.

3 Calculation of test statistics and modeling of UHECR flux

We now have to calculate the test statistics defined in Eq. (2.2). We also want to test its behavior for different compositions and magnetic field models, and therefore we need to generate Monte-Carlo event sets that follow these models. Both problems are solved by computing corresponding flux density maps. The goals, however, are different: in the case of test statistics we want to keep it as simple and model-independent as possible, while in the case of test UHECR sets we want to be as close to reality as we can achieve with available computational resources. The general steps are as follows. First, we model the source distribution in space and compute the flux, as a function of direction, as it would be observed at the borders of the Galaxy at a given energy E_k. The UHECR attenuation enters at this stage, but not the deflections. At the second step we add the deflections. To get the maps $\Phi_k(\theta, \mathbf{n})$ entering the test statistics Eq. (2.2) we apply a simple Gaussian smearing of width θ. In the case of flux maps used to generate model event sets, we apply a latitude-dependent smearing as described in the next Section and additionally process the flux through the regular Galactic magnetic field. To avoid confusion, we denote these maps as F_k. Finally, we use the model maps F_k to generate the test event sets which we need to study the behavior of the test statistics Eq. (2.2). We detail below these steps.

3.1 UHECR sources

As stated in the Introduction, we assume that the sources follow the large-scale matter distribution in the Universe, and that they are sufficiently numerous to be treated on statistical basis. Specifically, we assume that much more than one source is present in galaxy clusters and larger structures. While this is true in many models, there are source candidates that are more rare (for instance, powerful radio-galaxies) and for which this assumption does not hold. Note that the latter case physically corresponds to the situation when the UHECR propagation horizon, which is of order of a few tens of Mpc at highest energies, contains one or a few sources only. This case should be treated separately, which we leave for future work. These assumptions, together with the known distribution of galaxies up to a distance of $200-300$ Mpc, provide one with all the necessary information about the space distribution of UHECR sources.

In order to reconstruct the source distribution in space (and therefore, on the sky) under the above assumptions, we assign each galaxy an equal *intrinsic* luminosity in UHECR. In practice, we use the 2MRS galaxy catalog [21] which contains galaxy distances. We cut out dim galaxies with mag > 12.5 so as to obtain a flux-limited

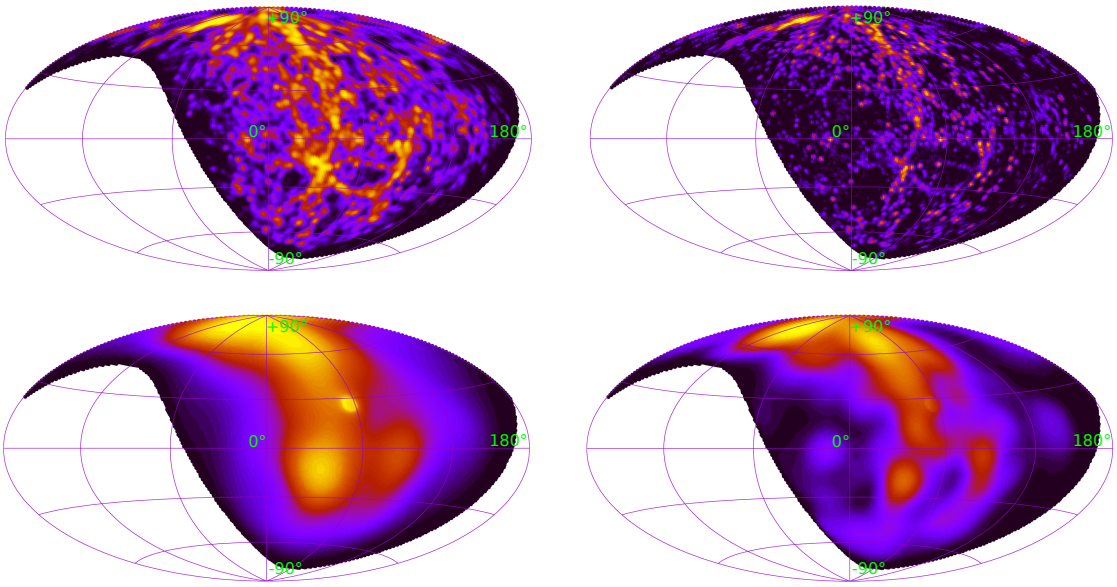

Figure 1. Examples of UHECR flux model maps Φ_k used for test statistic calculation. Proton attenuation length and uniform smearing of the sources is assumed: $\theta(100\text{ EeV}) = 1°$ (top) and $\theta(100\text{ EeV}) = 10°$ (bottom). Energies are $E_k = 57$ EeV (left) and $E_k = 100$ EeV (right). Maps are shown in galactic coordinates for TA SD field of view.

sample with a high degree of completeness, and eliminate galaxies beyond 250 Mpc. We assign progressively larger flux to more distant galaxies to compensate for the observational selection inherent in a flux-limited sample (see Ref. [22] for the exact procedure). In a similar way, we give more weight to the galaxies within $\pm 5°$ from the Galactic plane to compensate for the catalog incompleteness in this region. Finally, we assume that sources beyond 250 Mpc are distributed uniformly with the same mean density as those within this distance. We obtain in the end the space distribution of sources that is completely fixed.

3.2 UHECR propagation and deflection in magnetic fields

Contributions of individual sources to the observed flux are affected, apart from the trivial $1/r^2$ falloff, by the attenuation and deflections in magnetic fields. In practice these two effects can be separated. Most of the attenuation happens outside of the Galaxy where deflections are random and probably negligible all together, while in the Galaxy the deflections are important but the attenuation is negligible. We therefore calculate first, by making use of SimProp v2r4 code [23], the attenuated but non-deflected flux in a given energy bin as it arrives to the Galaxy borders. The flux in the energy bin k, calculated with the proton attenuation and smeared with the Gaussian function of the width θ, gives the flux map $\Phi_k(\theta, \mathbf{n})$ which enters the definition of our test statistics, Eq. (2.2). We show several examples of these maps in Fig. 1.

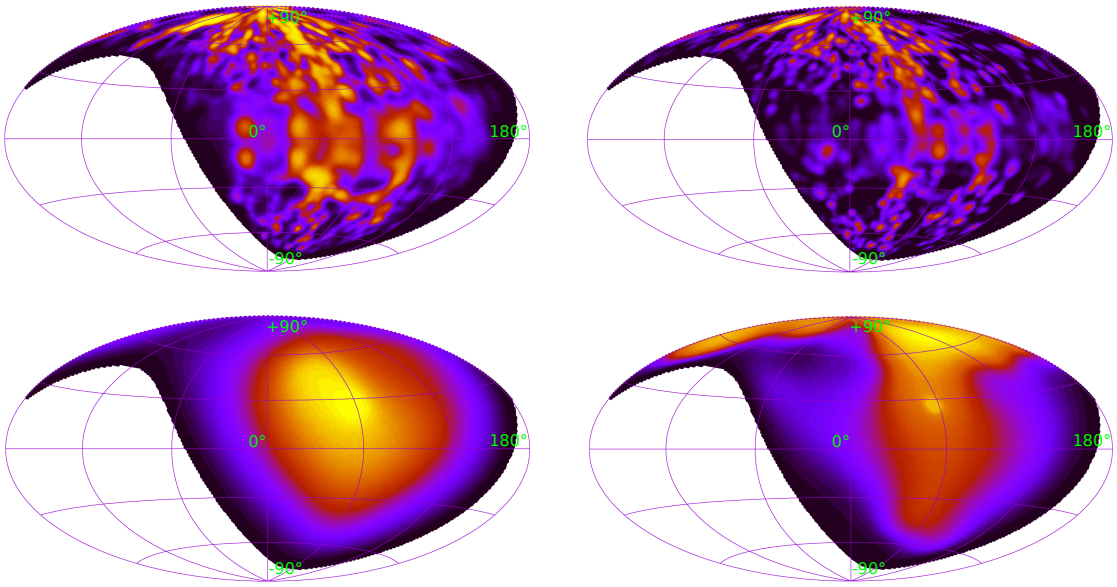

Figure 2. Examples of UHECR flux model maps, F_k used for mock UHECR sets simulation. Maps for protons with b-dependent smearing of the sources and *regular GMF effect*: $E = 57$ EeV (top left) and $E = 100$ EeV (top right). Maps for iron with b-dependent smearing of the sources and *regular GMF effect*: $E = 57$ EeV (bottom left) and $E = 100$ EeV (bottom right). Maps are shown in galactic coordinates for TA SD field of view.

For the generation of test event sets we need flux maps computed with the attenuation corresponding to different compositions. While straightforward in principle, the calculation of attenuation in the general case is fairly complicated as different species have different attenuation lengths and produce different sets of secondaries. Leaving the general treatment for future study, we simplify the problem by restricting ourselves to a proton-iron mix as the injected composition. This choice has two advantages. First, the proton-iron mix can be treated in the attenuation-only approximation, while secondaries can be neglected. Indeed, protons produce no secondaries (except very small number of gamma-rays and neutrinos that do not affect the general flux picture [24–26]). For iron nuclei the attenuation length is larger than for all its secondaries [27–29]. Furthermore, secondary protons from iron propagation have a factor ~ 50 lower energies than the primary nuclei and drop out from the high-energy range $E \gtrsim 10$ EeV that we consider in what follows. Second, the iron nuclei are deflected in magnetic fields stronger than all their secondaries, which makes the event distribution more uniform, and therefore conclusions based on anisotropies are conservative. The attenuation curves for protons and iron are obtained by fitting the results of SimProp v2r4 [23] simulations in the same way as in Ref. [17]. Note that we do not vary the injection spectrum of UHECR while calculating the flux maps, rather we fix it to the power-law with the spectral index $\alpha = -2.5$ and no cut-off. At the same time we assume the simulated mock event sets to follow the observed spectrum, see Sec. 3.3.

While this is a reasonable approximation, it is not entirely self-consistent: in the exact calculation the injection spectrum should be fitted to the observed one within a given composition model. We think, however, that for the estimate of the sensitivity of the method our approximation is sufficient.

The next step, which is only needed for the model maps F_k, is correcting the flux that arrives at the borders of the Galaxy by the deflections in the Galactic magnetic fields. The latter has regular and random components. For the regular field we take one of the two models [13, 14]. Both models give the regular magnetic field everywhere in the Galaxy as a function of a large number of parameters whose values are determined by fitting to the observational data. In each case we adopt the best fit values of these parameters as given in Refs. [13, 14]. Given the magnetic field, we convert the flux density outside of the Galaxy into the observed flux density as follows. To determine the observed flux density in a given direction $\mathbf{n}$ for a given species of charge q and given energy bin we back-track a particle of charge $-q$ and corresponding energy launched in the direction $\mathbf{n}$ through the galactic magnetic field until it leaves the Galaxy in some other direction $\mathbf{n}'$. The observed flux density in the direction $\mathbf{n}$ is given by the external flux density in the direction $\mathbf{n}'$. The total flux map in a given energy bin is the weighted sum of maps for individual species.

The deflections in random magnetic fields, both Galactic and extragalactic, have an effect of smearing of the flux density. The smearing is proportional to the combination Bq/E and is different for different UHECR species and energies E. If the random magnetic field was direction-independent the smearing would have been uniform over the sky. This is what we have adopted for the definition of the test statistics. Because of the presence of the Galactic random field which has a space-dependent magnitude, in reality the random deflections depend on the direction. We take this effect into account when generating the test event sets. The dependence of mean deflections $\sqrt{\langle\theta^2\rangle}$ (equivalently, the smearing angle) on the Galactic latitude has been estimated from the dispersion of Faraday rotation measures of extragalactic sources in Ref. [30] where the following empiric relation has been obtained for protons of $E = 40$ EeV:

$$\sqrt{\langle\theta^2\rangle} \leq \frac{1^\circ}{\sin^2 b + 0.15} \tag{3.1}$$

We conservatively adopt this relation treating it as the equality (i.e, assuming maximum deflections). For other species and energies we rescale it according to magnetic rigidity.

When the smearing is non-uniform and not small, there is a subtlety in how to implement it in a way that is accurate enough and not too complicated. A technically simplest option — to apply the full smearing by a latitude-dependent angle θ at once — is inaccurate at large gradients of θ as it would convert a point source into a circular distribution while in reality a deformed one is expected. We apply instead a series of N (in practice $N \sim 10$) *smaller identical smearings* where the smearing angle at one step $\sim \theta/\sqrt{N}$ is normalized in such a way that the result is identical to the one-step smearing by θ in the direction-independent case. Finally, we apply the additional uniform smearing by 1° to account for experiment's angular resolution. It only slightly

affects proton maps at high energies in the Galactic pole regions where the deflections due to random and regular magnetic fields are smaller than 1°. Note that if random deflections in the extragalactic fields are non-negligible contrary to what we assume here, they can also be added at this step. Several examples of resulting model flux maps F_k are shown in Fig. 2.

When we study the sensitivity of our method below in Secs. 4,5 we generate model flux maps using the regular magnetic field of Ref. [13] and the random field given by Eq. (3.1). In order to test the dependence of the sensitivity on the magnetic field parameters we also include in Sec.5.2 the field of Ref. [14]. For both models, we vary independently the overall magnitudes of regular and random fields.

3.3 Generation of mock UHECR event sets

Given model flux maps F_k, it is straightforward to generate a mock set of UHECR events as it would be detected by an EAS experiment at Earth. We modulate the all-sky flux map calculated as explained in Sec. 3.2 by the exposure function of the TA experiment, for which we take the geometrical exposure. Once multiplied by the exposure and normalized to a unit integral, the flux map is interpreted as probability distribution for the arrival directions, so the latter can be generated directly by throwing random events and accepting them with the probability given by the corresponding flux map at the position of the event.

The energies of events are generated randomly according to the actual TA SD spectrum [31]. Throughout the main part of this study we set the lower energy threshold of the mock events to be $E_{\rm min} = 57$ EeV, thus aiming to study the properties of UHECR in GZK-cutoff region. Note that this threshold energy is also adapted in the anisotropy studies by TA SD. In Section 5.3 we consider lower energy thresholds down to $E_{\rm min} = 10$ EeV and discuss the effect this has on the results.

4 Reconstruction of flux parameters with the test statistics

Before we can assess the sensitivity of our method in realistic cases it is instructive to check how it works for mock event sets generated with the same maps Φ_k as used in the definition of the test statistics (2.2), i.e. with uniform smearing only and without regular magnetic field effects. If we generate a mock event set with a given smearing parameter $\theta_{\rm th}$, we should recover the value of $\theta_{\rm th}$ by calculating the test statistics $TS(\theta)$ and finding its minimum. In the limit of large number of events $N_{\rm ev}$ the test statistic $TS(\theta)$ should follow the χ^2 distribution with one degree of freedom.

To check how well this picture is reproduced for a finite number of events in a set we generate a large number of sets with $N_{\rm ev}$ events, and calculate $TS(\theta)$ for each set. We record the position of the minimum $\theta_{\rm rec}$ and the width $\Delta\theta_{\rm rec}$ at $TS(\theta) = TS_{\rm min} + 1$ as corresponds to 1σ interval for the χ^2-distribution. If the minimum is not found in the range $0 \leq \theta < 200°$ we conclude that the given event set cannot be distinguished from an isotropic one by our TS and assign it a value $\theta_{\rm rec} = 200°$. Two examples of $TS(\theta)$ are shown in Fig. 3.

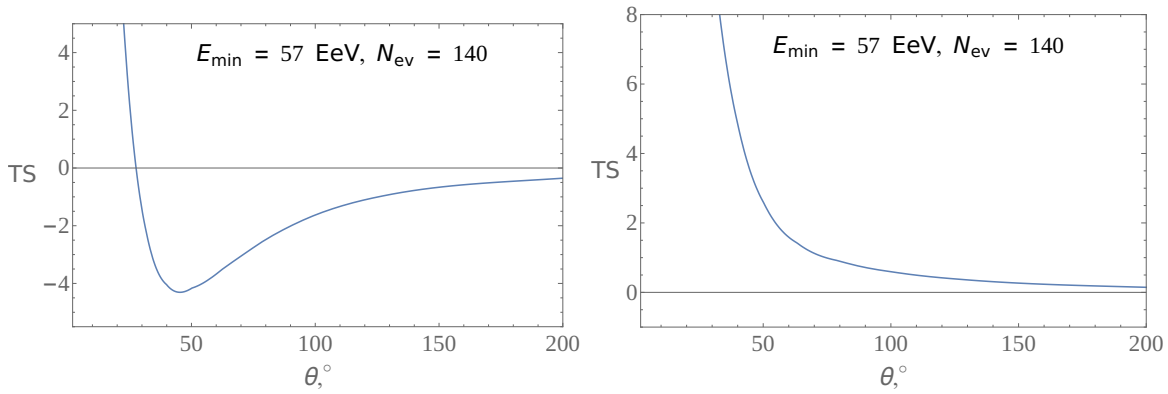

Figure 3. Examples of TS distribution for two different event sets with the same parameters: $E_{\rm min} = 57$ EeV and $N_{\rm ev} = 140$. *Left:* TS has a global minimum: $\theta_{\rm rec} = 45.4°$. *Right:* TS has no global minimum: $\theta_{\rm rec} = 200°$.

We now construct the distribution of the TS minima $\theta_{\rm rec}$ and compare its width with $\Delta\theta_{\rm rec}$. These distributions are shown in Fig. 4 for several numbers of events $N_{\rm ev}$ in mock sets. We found that already for $N_{\rm ev} \sim 100$ the deviation of the width of $\theta_{\rm rec}$ distribution from the mean $\Delta\theta_{\rm rec}$ is less then 3%, in agreement with the expectation from the χ^2-distribution. One can see in Fig. 4 that the distribution of $\theta_{\rm rec}$ for $N_{\rm ev} = 140$ is slightly asymmetric and its maximum is shifted from the input value $\theta_{\rm th} = 3.17°$ to smaller values. However, as $N_{\rm ev}$ increases the distribution becomes more narrow and symmetric, and the accuracy of reconstruction of $\theta_{\rm th}$ from this distribution increases.

Having checked that we can recover the input flux smearing parameter in the absence of the regular magnetic field, let us see how the test statistics (2.2) behaves when such a field is present. For this test we take the regular GMF model of Ref. [13] and fix its overall magnitude in such a way that the mean deflection in the regular field is 3 times larger than the mean random deflection which we keep the same as in the beginning of this Section. Note that this is a realistic ratio between the two contributions [30], but regular deflections themselves are about 3 times larger than would be for protons and best-fit GMF parameters of Ref. [13].

The results of the test are presented in Fig. 5 where on the left panel we show the comparison with the case of zero regular field, and on the right panel the behavior of the distribution with the number of events in the mock set, $N_{\rm ev}$. Notably, individual TS curves still have minima so that $\theta_{\rm rec}$ can be determined, and their distribution has a clear maximum, although shifted to larger angles. As in the case of no regular field, the resulting distributions tend to Gaussian ones as $N_{\rm ev}$ increases.

5 Results

5.1 Inference of the UHECR mass composition from the likelihood shape

The robustness of the likelihood shape to the presence of regular GMF opens a way for a new method of UHECR mass composition estimation. As it was shown, the position

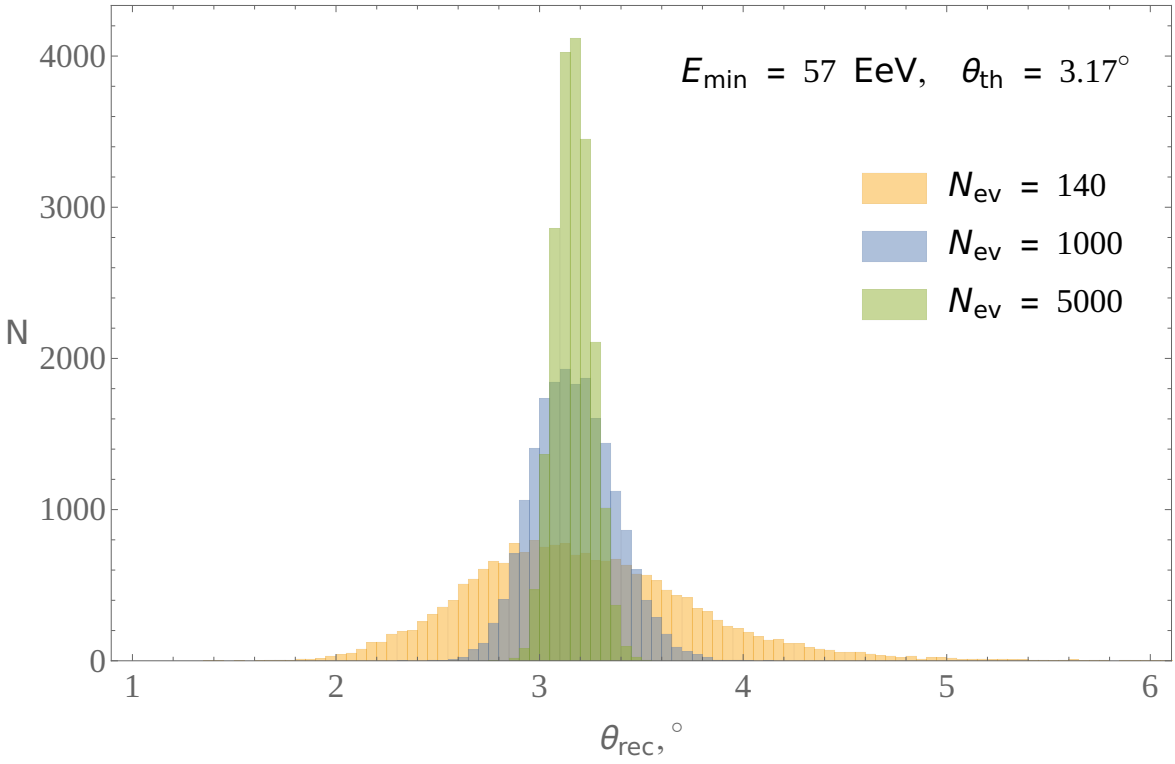

Figure 4. Distribution of TS minima, θ_{rec}, for event sets based on the same flux model map ($E_{\min} = 57$ EeV, $\theta_{\text{th}} = 3.17°$, no reg. GMF effect) but for different number of events in a set: $N_{\text{ev}} = 140$ (yellow histogram), $N_{\text{ev}} = 1000$ (blue histogram) and $N_{\text{ev}} = 5000$ (green histogram).

of the likelihood minimum, θ_{rec}, is the proxy of the primary particles deflection from their sources that is directly related to the charge of these particles. Therefore, by measuring θ_{rec} in the data one could estimate the mean charge of UHCER in a given sample. This estimation can be made by comparing the value of θ_{rec} for the data with the distribution of θ_{rec} in mock event sets of a particular UHECR composition model. Since we only have one number θ_{rec} determined from the data, the exact composition is impossible to determine because the same value of θ_{rec} may correspond to different composition models. Nevertheless, the composition can be constrained by excluding models where the measured value of θ_{rec} never occurs or occurs rarely.

To illustrate our method suppose a hypothetical experiment (we use the parameters of TA for concreteness) has observed N_{ev} events, calculated the test statistics (2.2) and found its minimum to be θ_{data}. What conclusions regarding the composition of UHECR can be deduced from that?

As already explained, in this paper we limit ourselves with a simplified approach where the UHECR consist of a proton-iron mixture. The aim is thus to constrain the fraction of protons and iron in this mix. Despite the simplification, the results of this approach may still be of practical importance as the upper bound on the proton

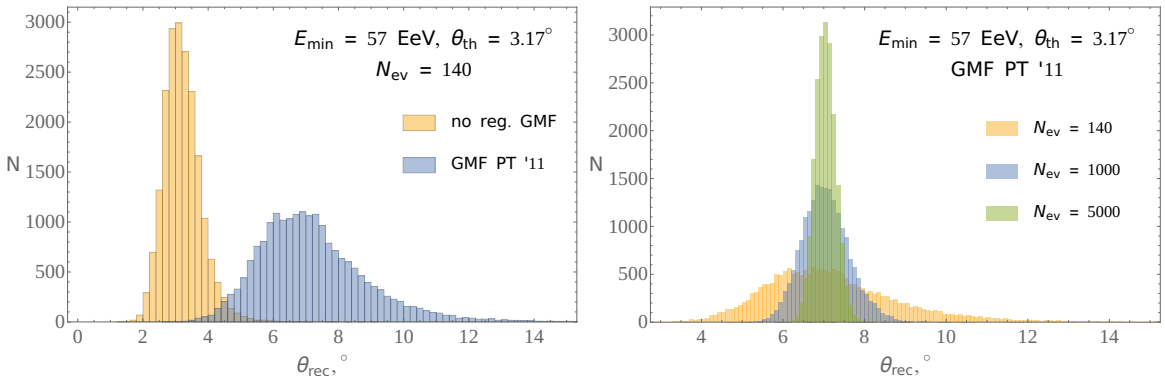

Figure 5. *Left:* Comparison of $\theta_{\rm rec}$ distribution for event sets based on the flux model maps with regular GMF effect (blue histogram) and without it (yellow histogram). Other event sets parameters are the same for both sets: $E_{\rm min} = 57$ EeV, $\theta_{\rm th} = 3.17°$ and $N_{\rm ev} = 140$. *Right:* Distributions of $\theta_{\rm rec}$ for event sets with regular GMF effect for different number of events in a set: $N_{\rm ev} = 140$ (yellow histogram), $N_{\rm ev} = 1000$ (blue histogram) and $N_{\rm ev} = 5000$ (green histogram). Other event set parameters are the same as for left picture.

fraction derived in this setup is conservative in the sense that it will hold if iron is replaced by lighter species, because the iron component drags the maximum of the $\theta_{\rm rec}$ distribution to larger values stronger than any other possible admixture. The same applies to the upper bound on the fraction of iron — the proton component pulls the maximum of $\theta_{\rm rec}$ to smaller values stronger than other nuclei.

We will present the results for different number of events $N_{\rm ev}$ roughly corresponding to the UHECR statistics already accumulated and expected in the future. The number of events with $E > 57$ EeV accumulated to date by the surface detector of the TA experiment is ~ 140, while with a recently constructed extension, TAx4 [32], one expects the tripling of this statistics in the next six years. At corresponding energies, the current statistics accumulated by the Pierre Auger surface detector is about ~ 1200 events [29]. Therefore, we present upper limits for the proton and iron fractions for $N_{\rm ev}$ equal to 140, 500 and 1200.

For each $N_{\rm ev}$ we generate 20000 mock event sets with energy-independent proton and iron fractions $P_{\rm p}$ and $P_{\rm Fe} = 1 - P_{\rm p}$, respectively. We repeat this procedure for various values of $P_{\rm p}$ and $P_{\rm Fe}$. The proton and iron events are generated from flux maps computed with corresponding attenuation functions. These maps are processed through the same GMF of Ref. [13] with the best fit parameters and charges 1 and 26 for proton and iron, respectively. They are then smeared with the latitude-dependent Gaussian width defined by Eq. (3.1) for protons at $E = 40$ EeV and rescaled according to the energy of the current bin and particle charge. No free parameters enter this calculation apart from the fractions $P_{\rm p}$ and $P_{\rm Fe}$. For every value of $P_{\rm p}$ we build a distribution of the minima of our test statistics, $\theta_{\rm rec}$. The illustrative examples of these distributions for three different values of $P_{\rm p}$ are shown in Fig. 6.

Given the assumed value of $\theta_{\rm data}$, we identify values of P_p such that either the right tail of the histogram $\theta_{\rm rec} > \theta_{\rm data}$ or the left tail $\theta_{\rm rec} < \theta_{\rm data}$ contains no more than

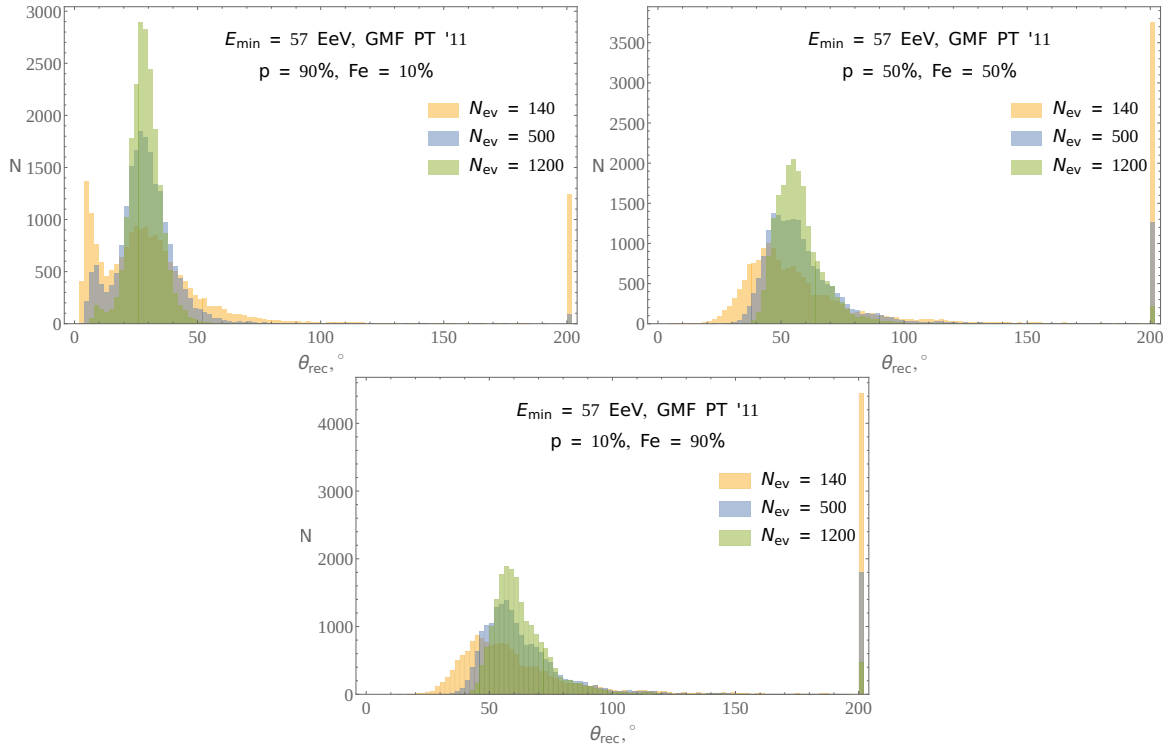

Figure 6. Distributions of $\theta_{\rm rec}$ for event sets with $E_{\rm min} = 57$ EeV, different constant p-Fe mix compositions and various numbers of events in a set: $P_{\rm p} = 90\%, P_{\rm Fe} = 10\%$ (top left), $P_{\rm p} = 50\%, P_{\rm Fe} = 50\%$ (top right) and $P_{\rm p} = 10\%, P_{\rm Fe} = 90\%$ (bottom). Numbers of events are $N_{\rm ev} = 140$ (yellow histogram), $N_{\rm ev} = 500$ (blue histogram) and $N_{\rm ev} = 1200$ (green histogram).

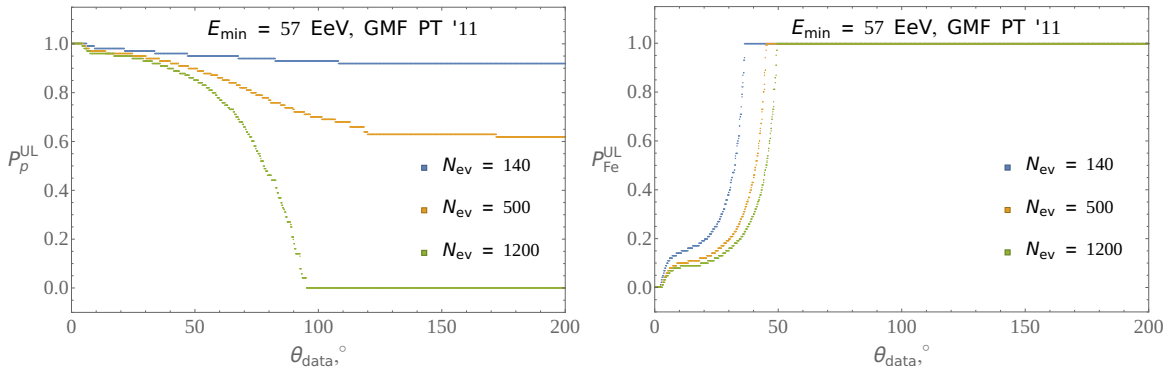

Figure 7. 95% C.L. upper-limits on the constant fractions of proton (left panel) and iron (right panel) in p-Fe mix as a function of $\theta_{\rm data}$. Numbers of events are $N_{\rm ev} = 140$ (blue line), $N_{\rm ev} = 500$ (yellow line) and $N_{\rm ev} = 1200$ (green line). $E_{\rm min} = 57$ EeV.

5% of occurrences. In the first case we conclude that the proton fraction P_p and larger ones are excluded at 95% C.L., while in the second that iron fraction $P_{\rm Fe} = 1 - P_{\rm p}$

$\theta_{\rm rec}$	$N_{\rm ev}$	$P_{\rm p}^{\rm UL}$ (95% C.L.)	$P_{\rm Fe}^{\rm UL}$ (95% C.L.)
3.0°	140	1.00	0.04
3.0°	500	1.00	0.01
3.0°	1200	1.00	0.00
40°	140	0.96	1.00
40°	500	0.93	0.45
40°	1200	0.90	0.30
200°	140	0.92	1.00
200°	500	0.62	1.00
200°	1200	0.00	1.00

Table 1. 95% C.L. upper-limits on fractions of protons, $P_{\rm p}$, and fraction of iron nuclei, $P_{\rm Fe}$, in p-Fe mix models with $P_{\rm p}$ and $P_{\rm Fe}$ not changing with energy. The limits are derived from the mock sets with various number of events and different values of TS minimum: $\theta_{\rm rec} = 3.0°$ (top panel), $\theta_{\rm rec} = 40°$ (middle panel) and isotropic set ($\theta_{\rm rec} = 200°$, bottom panel).

and larger ones are excluded at 95% C.L. The resulting constraints are plotted as a function of $\theta_{\rm data}$ in Fig. 7 We also summarize several numerical values of upper limits derived for three sample values of $\theta_{\rm data}$ in Table 1.

As expected, when $\theta_{\rm data}$ is large one cannot constrain the fraction of iron nuclei, while at small $\theta_{\rm data}$ no constraint on the fraction of protons can be set. Less obvious is that constraints on the fraction of iron are generally stronger than those on the fraction of protons, as is clear from the fact that the left tail of the $\theta_{\rm rec}$-distributions is steeper than the right one. The underlying reason is that an admixture of protons on a low-contrast mostly iron map has smaller effect on the test statistics than an admixture of iron on a higher-contrast mostly proton map.

So far we have been assuming that the composition does not change with energy. However, since the test statistics (2.2) depends differently on composition at different energies, our method may also be used to distinguish a composition evolving with energy from the constant composition. To illustrate this point we compare distributions of $\theta_{\rm rec}$ for several composition models: pure proton constant composition (M_1), proton-iron mix with constant $P_{\rm p} = 0.9$ (M_2), proton-iron mix with $P_{\rm p} = 0.9 \cdot (57\ {\rm EeV}/E)^2$ (M_3) and the main composition model from Ref. [3] — a mix of nitrogen and silicon (M_4). [1] We compare these models in pairs by choosing one model $M_{\rm test}$ as a "null hypothesis" (the one to be constrained, or test model) and another, $M_{\rm ref}$, as an "alternative hypothesis" (the reference model the data are assumed to follow). Following the standard definition of the statistical power we cut out 5%-tail of the null hypothesis distribution on the side where it overlaps most with the alternative one, and integrate the alternative distribution from the cut point to infinity to get the statistical power

[1] For the purpose of this illustration, we generate the flux maps for nitrogen and silicon nuclei assuming proton attenuation length which is larger than the actual one. The resulting maps are more proton-like (less contrast) than they should actually be, and our model comparison is therefore conservative — with the correct attenuation the models will be easier to distinguish.

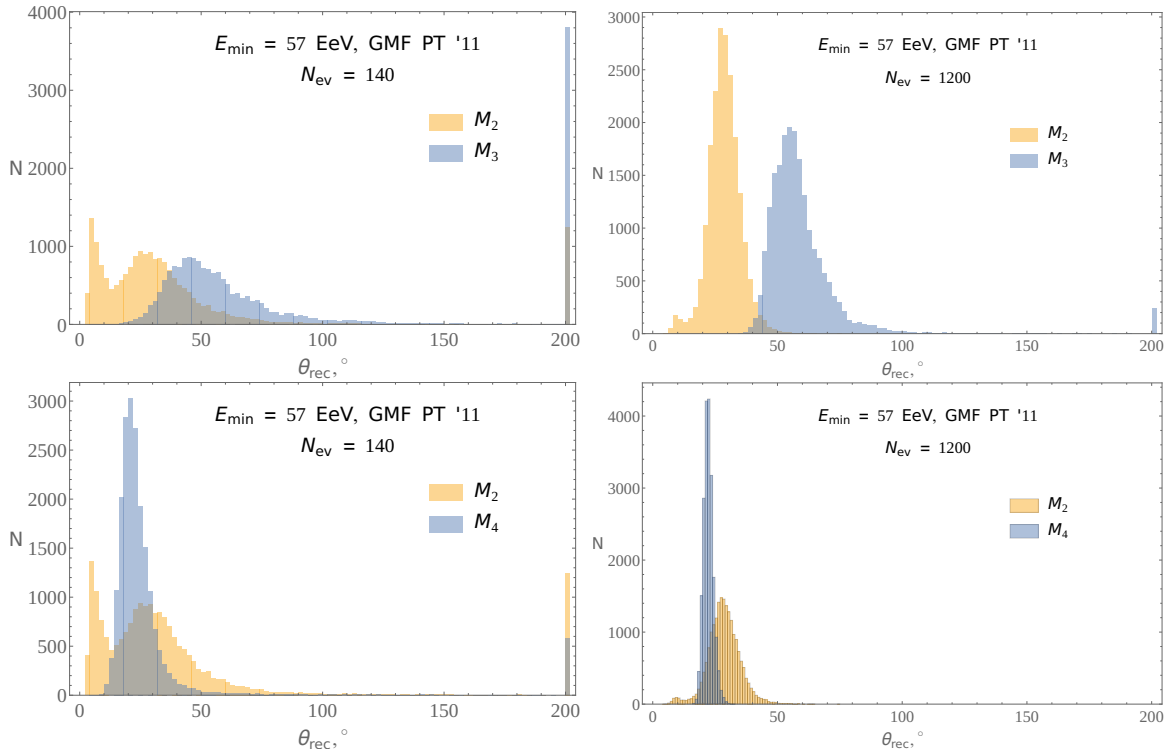

Figure 8. Examples of $\theta_{\rm rec}$ distributions overlap between M_2 and M_3 composition models for $N_{\rm ev} = 140$ (top left) and $N_{\rm ev} = 1200$ (top right) and between M_2 and M_4 composition models for $N_{\rm ev} = 140$ (bottom left) and $N_{\rm ev} = 1200$ (bottom right). See text for models description.

$P(M_{\rm ref}, M_{\rm test})$. The resulting value, $P(M_{\rm ref}, M_{\rm test})$, is interpreted as a chance to constrain the test model at 95% C.L. if the data follows the reference model. When two distributions overlap only slightly, the statistical power is close to 1.

The comparison of the models for various values of $N_{\rm ev}$ is shown in Fig. 8. The respective values of $P(M_{\rm ref}, M_{\rm test})$ are given in Tab. 2. One can see that at large enough statistics our method allows one to distinguish pure proton composition from a proton-dominated one, as well as proton dominated composition from a composition that becomes heavier with energy. However, even a small admixture of iron leads to significant decrease in the separation power (cf. $P(M_1, M_3)$ and $P(M_2, M_3)$) which, however, grows with statistics. It is also worth noting that one can certainly tell pure proton model M_1 from the medium-mass nuclei mix M_4, and the proton-iron mix M_2 from the medium-mass mix M_4 — with the reasonable confidence.

5.2 Uncertainties

The main uncertainty in our method of constraining composition comes from the Galactic magnetic field. It can be divided into three independent parts: the uncertainty of the regular field structure, of the overall regular magnetic field strength and of the random magnetic field strength. The latter two uncertainties are characterized by one

$N_{\rm ev}$	$P(M_1, M_2)$	$P(M_1, M_3)$	$P(M_2, M_3)$	$P(M_1, M_4)$	$P(M_2, M_4)$
140	0.95	1.00	0.58	1.00	0.25
500	1.00	1.00	0.89	1.00	0.50
1200	1.00	1.00	0.99	1.00	0.69

Table 2. Values of statistical power to constrain a test composition model at 95% C.L. if data follows a reference model, see text for explanation. Results for various number of events in a set are presented.

parameter each. The random magnetic field can be parameterized by $\theta_{\rm th}$ defined as the smearing angle at the Galactic pole for protons with energy $E = 100$ EeV (recall that we adopted latitude-dependent random deflections given by Eq. (3.1)) and rescaled according to particle charge and energy. So far we kept $\theta_{\rm th} = 0.4^\circ$ fixed, but now we will vary this parameter. The overall magnitude of the regular field can be parameterized by the dimensionless normalization factor Q with the value $Q = 1$ for the best-fit parameters used up to now. In Fig. 9 we vary these parameters from their reference values one at a time and show how this affects the distribution of $\theta_{\rm rec}$ for the pure proton composition model and the GMF of Ref. [13]. We also show the comparison of the two GMF models of Refs. [13, 14].

Next, we estimate the impact of these uncertainties on the composition constraints by calculating a relative difference ε between statistical powers calculated with reference and test GMF parameters. For instance, in case of $P(M2, M3)$ we define

$$\varepsilon = \frac{P_{\rm GMF_{test}}(M_2, M_3) - P_{\rm GMF_{ref}}(M_2, M_3)}{P_{\rm GMF_{ref}}(M_2, M_3)} \ . \tag{5.1}$$

First we reproduce the previous results for the regular GMF model of Ref. [14] as a test model, while keeping the absolute strength of random and regular GMF components fixed at their reference values $\theta_{\rm th} = 0.4^\circ$ and $Q = 1$. When testing two other uncertainties we fix the regular GMF model of Ref. [13] and change the parameters $\theta_{\rm th}$ and Q from their reference values one at a time. We consider the values $\theta_{\rm th} = 0.4^\circ, 0.8^\circ$ and $Q = 1, 2$. The results are summarized in Table 3. One can see that these uncertainties decrease with increasing statistics, as expected from the definition of the likelihood (2.2). Thus, once a GMF model is fixed, two different composition models yield peaks at different positions, although more statistics is needed to distinguish the same composition models for a larger GMF strength. The degeneracy between two composition models could occur only in the situation when GMF or EGMF is so large that average deflections in these models are larger then the experiment's field of view (about a half of the sky for TA), in which case both models would have peaks at the value of $\theta_{\rm rec}$ corresponding to isotropy. Therefore, the proposed method has a potential to separate the composition models irrespectively of which GMF model is assumed, provided that the event set is large enough.

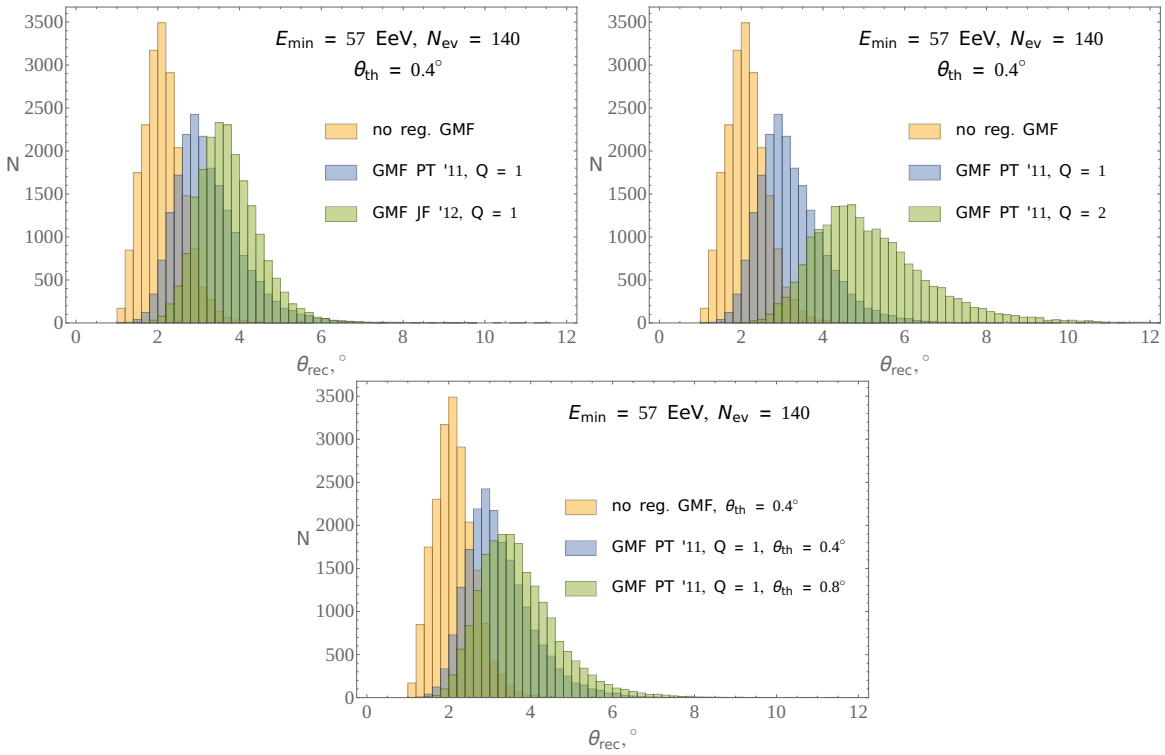

Figure 9. Comparison of $\theta_{\rm rec}$ distributions for various values of GMF parameters. *Top left:* no regular GMF vs. regular GMF model of Ref. [13] and model of Ref. [14], for both reg. GMF models $Q = 1$ and $\theta_{\rm th} = 0.4°$. *Top right:* regular GMF model of Ref. [13], $\theta_{\rm th} = 0.4°$, comparison of $Q = 1$ and $Q = 2$. *Bottom:* regular GMF model of Ref. [13], $Q = 1$, comparison of $\theta_{\rm th} = 0.4°$ and $\theta_{\rm th} = 0.8°$. Pure proton composition with $E_{\rm min} = 57$ Eev and $N_{\rm ev} = 140$ are imposed for all event sets.

$N_{\rm ev}$	ε, ΔGMF model	ε, $\Delta\theta_{\rm th}$	ε, ΔQ
140	-0.25	-0.16	-0.34
500	-0.23	-0.13	-0.28
1200	-0.10	-0.039	-0.13

Table 3. Impact of variation of magnetic field parameters on the method's statistical power between composition models M_2 and M_3 for various number of events in a set, see text for details.

5.3 Dependence on the lower energy threshold

So far we considered the energy range $E > 57$ EeV, but the same method can be applied at lower energies. This will address a different physics question, namely what is the composition in that energy range. However, it is instructive to compare the performance of the method for one and the same composition model but with different energy thresholds, $E_{\rm min}$. The UHECR statistics at lower energies increases, but

$E_{\rm min}$, EeV	$N_{\rm ev}$	$P(M_5, M_6)$	$P(M_5, M_7)$	$P(M_8, M_9)$	$P(M_8, M_{10})$
57	140	0.13	0.57	0.09	1.00
10	5000	0.17	0.94	0.10	1.00

Table 4. Values of statistical power to constrain a test composition model at 95% C.L. if data follows a reference model, see text for explanation. Comparison of results for two different values of $E_{\rm min}$. Binning over energy is 10 logarithmic bins per decade in both cases.

the events deflections and their uncertainties grow as well. Therefore, it is difficult to estimate the change in a method performance *a priori*. We estimate the sensitivity using simulations for $E > 10$ EeV with the same energy binning of 10 bins per decade. We fix the size of the sample to 5000 events, which approximately corresponds to the recent statistics of TA SD at these energies, and also corresponds to 140 events in a sample with $E > 57$ EeV that was studied in the main part of this work. Like in Section 5.1 we calculate the statistical power which determines a chance to discriminate one composition model from another. Specifically, we consider 6 proton-iron mix models with power-law change of the proton fraction $P_{\rm p}$ with energy: three models with $P_{\rm p} = 0.75$ at 10 EeV and different power-law indices $P_{\rm p} = {\rm const}$ (M_5), $P_{\rm p} \sim E^{-0.1}$ (M_6) and $P_{\rm p} \sim E^{0.1}$ (M_7), and three models with $P_{\rm p} = 0.5$ at 10 EeV, also with different power-law behaviours $P_{\rm p} = {\rm const}$ (M_8), $P_{\rm p} \sim E^{-0.5}$ (M_9) and $P_{\rm p} \sim E^{0.5}$ (M_{10}). We choose the model M_5 as the reference model for the models M_6 and M_7, and the model M_8 as the reference one for the models M_9 and M_{10}. The results are shown in Tab. 4.

One can see that at least in the case of a simple power-law composition evolution, lowering the energy threshold is beneficial both in the case of increasing and decreasing proton fraction. In both cases lower energy bins do not spoil the separation achieved at higher energies, but can give a non-zero or even dominant contribution to the total separation power of the method.

6 Conclusions

In summary, in this paper we proposed a quantitative method to assess composition of UHECR by using information on their arrival directions and energies, under the assumption that sources follow the large-scale matter distribution in the Universe. The key point of the proposal is calculation of the typical deflection angle with respect to the LSS source model. This angle is defined as a minimum $\theta_{\rm rec}$ of the likelihood function $TS(\theta)$, Eq. (2.2). It should be calculated for the data and compared to the same quantity calculated for the composition model in question. We have shown by applying Eq. (2.2) to realistic mock event sets that the minimum is robust to the presence of the regular GMF and to mixed compositions, and therefore its position can be used to discriminate between composition models.

To quantify the discriminating power of the test we calculated the standard statistical power for several pairs of the null-alternative models. We found that the statistical power reaches 1 (the maximum value) or gets close to 1 in a number of cases, in par-

ticular, when the alternative model is a pure proton composition. In other words, the distribution of $\theta_{\rm rec}$ for pure proton model is well separated from other models. This means that the pure proton composition has good chances to be ruled out, in agreement with the results of Ref. [17]. In all cases we found that the discriminative power increases with the statistics of UHECR regardless of the assumed GMF model.

Finally, we have investigated the dependence of the results on the unknown parameters, of which most important are those characterizing magnetic fields. We have seen that, while changing these parameters within reasonable limits does change the typical deflection angle, this change is not so large as to make it impossible to constrain the composition parameters or discriminate between models. In either case the conclusion strengthens with the accumulation of statistics.

Our method has several advantages: it is based exclusively on measured UHECR arrival directions and energies of events which are most reliably determined from the reconstruction of air showers; it is not sensitive to the details of the regular GMF; it can give conclusive results even at highest energies where use of other methods of composition study is limited by low UHECR statistics.

These advantages come at a price of having only one parameter determined from the data, so in general only one combination of variables characterizing composition can be determined/constrained. Note however that more parameters (in particular, those characterizing magnetic fields) can be incorporated into Eq. (2.2) in a straightforward way, trading model independence for additional information on composition.

The crucial assumption of our method is that sources follow the matter distribution. We also assumed that they can be treated on statistical basis. If the sources are too rare to populate nearby galaxy clusters, Eq. (2.2) can still be used to define a test statistics. We expect that the method will still work but will have a lower sensitivity, because in this case the sources will still correlate with the concentrations of matter. Given a high isotropy of the UHECR data this case is not expected as it would correspond to only a few sources contributing to the flux. We leave the quantitative analysis of this case for future.

Acknowledgments

We would like to thank S. Troitsky, O. Kalashev and V. Rubakov for useful discussions and helpful comments on the manuscript. This work is supported in part by the IISN, convention 4.4501.18.

References

[1] Telescope Array collaboration, R. Abbasi et al., *Depth of Ultra High Energy Cosmic Ray Induced Air Shower Maxima Measured by the Telescope Array Black Rock and Long Ridge FADC Fluorescence Detectors and Surface Array in Hybrid Mode*, *Astrophys. J.* **858** (2018) 76, [1801.09784].

[2] Telescope Array collaboration, R. Abbasi et al., *Mass composition of ultrahigh-energy cosmic rays with the Telescope Array Surface Detector data*, *Phys. Rev. D* **99** (2019) 022002, [1808.03680].

[3] Pierre Auger collaboration, A. Aab et al., *Combined fit of spectrum and composition data as measured by the Pierre Auger Observatory*, *JCAP* **04** (2017) 038, [1612.07155].

[4] Pierre Auger collaboration, A. Aab et al., *Inferences on mass composition and tests of hadronic interactions from 0.3 to 100 EeV using the water-Cherenkov detectors of the Pierre Auger Observatory*, *Phys. Rev. D* **96** (2017) 122003, [1710.07249].

[5] A. Neronov and I. Vovk, *Evidence for strong extragalactic magnetic fields from Fermi observations of TeV blazars*, *Science* **328** (2010) 73–75, [1006.3504].

[6] A. Taylor, I. Vovk and A. Neronov, *Extragalactic magnetic fields constraints from simultaneous GeV-TeV observations of blazars*, *Astron. Astrophys.* **529** (2011) A144, [1101.0932].

[7] M. Pshirkov, P. Tinyakov and F. Urban, *New limits on extragalactic magnetic fields from rotation measures*, *Phys. Rev. Lett.* **116** (2016) 191302, [1504.06546].

[8] K. Dolag, D. Grasso, V. Springel and I. Tkachev, *Constrained simulations of the magnetic field in the local Universe and the propagation of UHECRs*, *JCAP* **01** (2005) 009, [astro-ph/0410419].

[9] H. M. Courtois, D. Pomarede, R. B. Tully and D. Courtois, *Cosmography of the Local Universe*, *Astron. J.* **146** (2013) 69, [1306.0091].

[10] M. Haverkorn, *Magnetic Fields in the Milky Way*, 1406.0283.

[11] J. Han, R. Manchester, A. Lyne, G. Qiao and W. van Straten, *Pulsar rotation measures and the large-scale structure of Galactic magnetic field*, *Astrophys. J.* **642** (2006) 868–881, [astro-ph/0601357].

[12] X. Sun, W. Reich, A. Waelkens and T. Enslin, *Radio observational constraints on Galactic 3D-emission models*, *Astron. Astrophys.* **477** (2008) 573, [0711.1572].

[13] M. S. Pshirkov, P. G. Tinyakov, P. P. Kronberg and K. J. Newton-McGee, *Deriving global structure of the Galactic Magnetic Field from Faraday Rotation Measures of extragalactic sources*, *Astrophys. J.* **738** (2011) 192, [1103.0814].

[14] R. Jansson and G. R. Farrar, *A New Model of the Galactic Magnetic Field*, *Astrophys. J.* **757** (2012) 14, [1204.3662].

[15] Pierre Auger collaboration, A. Aab et al., *Observation of a Large-scale Anisotropy in the Arrival Directions of Cosmic Rays above* 8×10^{18} *eV*, *Science* **357** (2017) 1266–1270, [1709.07321].

[16] Telescope Array collaboration, R. Abbasi et al., *Indications of Intermediate-Scale Anisotropy of Cosmic Rays with Energy Greater Than 57 EeV in the Northern Sky Measured with the Surface Detector of the Telescope Array Experiment*, *Astrophys. J. Lett.* **790** (2014) L21, [1404.5890].

[17] A. di Matteo and P. Tinyakov, *How isotropic can the UHECR flux be?*, *Mon. Not. Roy. Astron. Soc.* **476** (2018) 715–723, [1706.02534].

[18] E. Armengaud, G. Sigl, T. Beau and F. Miniati, *Crpropa: a numerical tool for the propagation of uhe cosmic rays, gamma-rays and neutrinos*, *Astropart. Phys.* **28** (2007) 463–471, [astro-ph/0603675].

[19] R. Aloisio, D. Boncioli, A. Grillo, S. Petrera and F. Salamida, *SimProp: a Simulation Code for Ultra High Energy Cosmic Ray Propagation*, *JCAP* **10** (2012) 007, [1204.2970].

[20] O. Kalashev and E. Kido, *Simulations of Ultra High Energy Cosmic Rays propagation*, *J. Exp. Theor. Phys.* **120** (2015) 790–797, [1406.0735].

[21] J. P. Huchra et al., *The 2MASS Redshift Survey - Description and Data Release*, *Astrophys. J. Suppl.* **199** (2012) 26, [1108.0669].

[22] H. B. Koers and P. Tinyakov, *Flux calculations in an inhomogeneous Universe: weighting a flux-limited galaxy sample*, *Mon. Not. Roy. Astron. Soc.* **399** (2009) 1005, [0907.0121].

[23] R. Aloisio, D. Boncioli, A. Di Matteo, A. F. Grillo, S. Petrera and F. Salamida, *SimProp v2r4: Monte Carlo simulation code for UHECR propagation*, *JCAP* **11** (2017) 009, [1705.03729].

[24] G. B. Gelmini, O. E. Kalashev and D. V. Semikoz, *GZK Photons Above 10-EeV*, *JCAP* **11** (2007) 002, [0706.2181].

[25] G. B. Gelmini, O. Kalashev and D. V. Semikoz, *Gamma-Ray Constraints on Maximum Cosmogenic Neutrino Fluxes and UHECR Source Evolution Models*, *JCAP* **01** (2012) 044, [1107.1672].

[26] R. Alves Batista, D. Boncioli, A. di Matteo and A. van Vliet, *Secondary neutrino and gamma-ray fluxes from SimProp and CRPropa*, *JCAP* **05** (2019) 006, [1901.01244].

[27] J. Puget, F. Stecker and J. Bredekamp, *Photonuclear Interactions of Ultrahigh-Energy Cosmic Rays and their Astrophysical Consequences*, *Astrophys. J.* **205** (1976) 638–654.

[28] S. Lee, *On the propagation of extragalactic high-energy cosmic and gamma-rays*, *Phys. Rev. D* **58** (1998) 043004, [astro-ph/9604098].

[29] Pierre Auger, Telescope Array collaboration, A. di Matteo et al., *Full-sky searches for anisotropies in UHECR arrival directions with the Pierre Auger Observatory and the Telescope Array*, *PoS* **ICRC2019** (2020) 439, [2001.01864].

[30] M. S. Pshirkov, P. G. Tinyakov and F. R. Urban, *Mapping UHECRs deflections through the turbulent galactic magnetic field with the latest RM data*, *Mon. Not. Roy. Astron. Soc.* **436** (2013) 2326, [1304.3217].

[31] D. Ivanov, *TA Spectrum Summary*, *PoS* **ICRC2015** (2016) 349.

[32] Telescope Array collaboration, E. Kido, *Status and prospects of the TAx4 experiment*, *PoS* **ICRC2019** (2020) 312.